
CNN Denoisers As Non-Local Filters: The Neural Tangent Denoiser

Julián Tachella*
 School of Engineering
 University of Edinburgh
 Julian.Tachella@ed.ac.uk

Junqi Tang
 School of Engineering
 University of Edinburgh
 J.Tang@ed.ac.uk

Michael E. Davies
 School of Engineering
 University of Edinburgh
 Mike.Davies@ed.ac.uk

Abstract

Convolutional Neural Networks (CNNs) are now a well-established tool for solving computational imaging problems. Modern CNN-based algorithms obtain state-of-the-art performance in diverse image restoration problems. Furthermore, it has been recently shown that, despite being highly overparametrized, networks trained with a single corrupted image can still perform as well as fully trained networks, a phenomenon encapsulated in the *deep image prior*. We introduce a novel interpretation of denoising networks with no clean training data in the context of the neural tangent kernel (NTK), elucidating the strong links with well-known non-local filtering techniques, such as non-local means or BM3D. The filtering function associated with a given network architecture can be obtained in closed form without need to train the network, being fully characterized by the random initialization of the network weights. While the NTK theory accurately predicts the filter associated with networks trained using standard gradient descent, our analysis shows that it falls short to explain the behaviour of networks trained using the popular Adam optimizer. The latter achieves a larger change of weights in hidden layers, adapting the non-local filtering function during training. We evaluate our findings via extensive image denoising experiments.

1 Introduction

Convolutional neural networks are now ubiquitous in deep learning solutions for computational imaging and computer vision, ranging from image restoration tasks such as denoising, deblurring, inpainting and superresolution, to image reconstruction tasks such as computed-tomography [1] and magnetic resonance imaging (MRI). A standard approach consists of training the networks with a large dataset of clean images, which may not be available for many important applications such as dynamic MRI [2]. Hence, a line of research has been devoted to reduce (or remove completely) the need for clean training images [3; 4; 5]. Ulyanov *et al.* [6] discovered that training a CNN only with a single corrupted image (the one being restored) could still achieve competitive reconstructions in comparison to fully trained networks, naming this phenomenon the deep image prior (DIP). In this setting, the number of weights (e.g., 2,000,000 for a U-Net CNN [6; 7]) is much larger than the number of pixels in the training image (e.g., 50,000 pixels of a standard 128×128 color image). The clean version of the corrupted image is obtained by early-stopping the optimization process before the network fully matches the noisy image. This surprising result raises the natural question: how, amongst all possible optimization trajectories towards the multiple global minima of the training loss, the procedure consistently provides close to state-of-the-art reconstructions?

Despite its surprisingly good performance, the DIP provides comparable or slightly worse denoising results than classical patch-based non-local filtering techniques, such as non-local means (NLM) [8]

*The codes associated with this work are available at gitlab.com/Tachella/neural_tangent_denoiser.

or BM3D [9], which also only have access to the corrupted image. Moreover, the DIP is more computationally intensive, as the denoising process involves training a very large network. Subsequent questions then arise: is the neural network performing a similar filtering process? Can we avoid the slow training, and apply this filter in a more direct way? Denoising is generally considered as the fundamental building block of any image restoration problem. In many applications, CNNs are used to perform denoising steps, either in unrolled schemes [1] or in the context of plug-and-play methods [10; 11]. Hence, understanding better the bias of CNNs towards clean images is the first step towards more general imaging problems.

On another line of work, researchers have also observed that increasing the amount of overparametrization does not necessarily harm the generalization of the network [12] in the context of classification. Recently, Jacot *et al.* showed that overparametrized neural networks trained with (stochastic) gradient descent (GD) converge to a Gaussian Process as the number of weights tends to infinity, with a kernel that depends only on the architecture and variance of the random initialization, named the neural tangent kernel (NTK) [13]. While the properties and accuracy of the kernel were analyzed for image classification [14], to the best of our knowledge, little is known in the context of high-dimensional image restoration with no clean data. Can this theory explain the DIP phenomenon?

In this paper, we study overparametrized convolutional networks and their associated neural tangent kernel in the context of the image denoising, formalizing strong links with classical non-local filtering techniques, but also analyzing the short-comings of this theory to fully explain the results obtained by the DIP. The main contributions of this paper are as follows:

1. We show that GD trained CNN denoisers with a single corrupted image (placed both at the input and as a target) in the overparametrized regime equate to performing an existing iterative non-local filtering technique known as *twicing* [15], where the non-local filter, which we name the neural tangent denoiser (NTD), is characterized by the architectural properties of the network. Moreover, we show that efficient filtering can be performed directly without the CNN, using the Nyström approximation [16].
2. We demonstrate that for the DIP, when independent and identically distributed (iid) noise is placed at the input of the network, the NTD is not able to explain the networks excellent performance. We link this short-coming to the choice of the optimization algorithm, and not a finite network width effect. When trained with GD the DIP has poor performance as predicted, and maintains a fixed NTD filter throughout. However training with the popular Adam optimizer as in the original DIP is able to adapt the filter with non-local information from the target image.
3. We evaluate our findings with a series of denoising experiments, showing that the fixed non-local filter associated with gradient descent performs significantly better when the corrupted image is placed at the input, whereas the Adam optimizer effectively adapts the filter during training, providing good results for both scenarios.

The paper is organized as follows: Section 2 enumerates previous works related to our findings. Section 3 introduces some basic concepts and notation. Section 4 presents the filtering function associated with overparametrized CNNs trained with gradient descent. The adaptation related to the Adam optimizer is discussed in Section 5. Finally, Section 6 illustrates the differences with several examples.

2 Related Work

Neural networks as Gaussian Processes Neal showed that a randomly initialized fully-connected networks converge to Gaussian Process [17]. This result was recently extended to the convolutional case [18]. Jacot *et al.* showed that the network remains a Gaussian Process throughout gradient descent training, but with a different kernel, the NTK [13]. Arora *et al.*, studied the kernel of a convolutional architecture for image classification [14], while Yang extended these results to a wider set of architectures [19]. All these works focus on classification with a set of training pairs of images and labels, whereas we study high-dimensional regression (denoising) with no clean training data.

Non-local (global) filtering A powerful class of denoisers in image processing use patch-based filtering, e.g. NLM [8] and BM3D [9]. Milanfar studied these from a kernel function perspec-

tive [15], identifying the associated affinity (kernel) matrices, along with different iterative denoising techniques.

Self-supervised image restoration In Noise2Noise [3], the authors show that training a denoising network with noisy targets can achieve similar performance to a network trained with clean targets. Similarly to the DIP, Noise2Void [4] and Noise2Self [5] present a self-supervised training procedure that achieves good performance, even with a single noisy image.

Deep image prior interpretations Cheng *et al.* [20], analyzed the spatial (i.e., low-pass) filter associated to a CNN at initialization, following the Gaussian Process interpretation of [17]. Our work differs significantly from theirs, as we also study the denoising behaviour during training. In contrast to the spatial filter in [20], the induced filters studied here are dependent on non-local information of the corrupted image, hence providing competitive performance to other patch-based methods.

3 Preliminaries

3.1 Convolutional neural networks

An L -layer vanilla² convolutional neural network with c channels at each hidden layer is defined as

$$a_i^1(x) = W_{i,1}^1 x \quad i = 1, \dots, c \quad (1)$$

$$a_i^\ell(x) = \sum_{j=1}^c W_{i,j}^\ell \phi(a_j^{\ell-1}(x)) \quad \ell = 2, \dots, L-1 \quad i = 1, \dots, c \quad (2)$$

$$z(x) = \sum_{j=1}^c W_{1,j}^L \phi(a_j^{L-1}(x)) \quad (3)$$

where $\phi : \mathbb{R}^d \mapsto \mathbb{R}^d$ is an element-wise activation function, $a_i^\ell \in \mathbb{R}^d$ are the i th channel preactivations at layer ℓ , $W_{i,j}^\ell \in \mathbb{R}^{d \times d}$ are circulant matrices associated with convolution kernels of size $r \times r$ with trainable parameters $\{w_{i,j,\alpha}^\ell : \alpha = 1, \dots, r^2\}$, the input and output are vectorized images of d pixels, denoted as $x \in \mathbb{R}^d$ and $z \in \mathbb{R}^d$ respectively. We focus on restoration with no clean training data, where only the corrupted image y is available as a training target. For the input there are 2 options:

1. Corrupted image: we place the noisy target as the input, i.e., $x = y$, e.g., [4; 5].
2. Noise: the input is assigned with iid noise, i.e., $x \sim \mathcal{N}(0, I)$, i.e., the DIP setting [6].

As there is a single input to the network, we will drop the dependence of z with respect to x for the sake of clarity, only focusing on the dependence with respect to the weights, denoted as $z(w)$, where the high-dimensional vector w contains all individual weights $w_{i,j,\alpha}^\ell$. We assume that the weights of the network are drawn iid using the standard *He initialization* [21], $w_{i,j,\alpha}^\ell \sim \mathcal{N}(0, \frac{\sigma_w^2}{r^2 c})$, which avoids vanishing or divergent outputs in deep networks, where σ_w^2 is chosen depending on the non-linearity [22], e.g., $\sigma_w^2 = 2$ for ReLU. As in most image restoration problems, we assume training is performed on the squared loss, defined as $\mathcal{L}(w) = \frac{1}{2} \|z(w) - y\|_2^2$. The DIP minimizes the loss using Adam [23], early-stopping before the network overfits the corrupted image y .

3.2 Non-local denoisers

Multiple existing non-local collaborative filtering techniques [15], such as the well-known NLM, BM3D or LARK [24], consist in computing a filtering matrix W with the (i, j) th entry related to the affinity between a (noisy) image patch x_i centered at pixel i and another (noisy) image patch x_j centered at pixel j , with $x = y$. For example, the NLM affinity function³ with patch size of $r \times r$ and

²While our derivations focus on a simple CNN structure for the sake of clarity of the presentation, the analysis can be extended to account for multiple channels at the input and output (e.g., RGB images), biases, skip connections, downsampling and upsampling operations, see Appendices A, E and F.

³There is a subtle, but important point: the NLM filter matrix is normalized [15] as $W' = \text{diag}(1^T W) W$.

parameter σ^2 is

$$[W]_{i,j} = k_{\text{NLM}}(x_i, x_j) = e^{-\frac{\|x_i - x_j\|_2^2}{\sigma^2}} \quad (4)$$

The most basic denoising procedure⁴ consists of applying W directly to the noisy image $z = Wy$. However, the performance can be improved using an iterative procedure named *twicing* [15],

$$z^{t+1} = z^t + W(y - z^t) \quad (5)$$

which trades bias for variance, starting with a blurry estimate and converging towards the noisy target y as $t \rightarrow \infty$. As with the DIP, the procedure is early-stopped to avoid overfitting the noise.

4 The Neural Tangent Denoiser

The seminal work in [13], and subsequent works [25; 19; 14], pointed out that as the number of parameters goes to infinity, which equates to taking $c \rightarrow \infty$, a network trained with gradient descent and learning rate η of order⁵ $\mathcal{O}(c^{-1})$, leads to a vanishingly small change of each individual weight [25; 14]

$$\max_t |(w_{i,j,\alpha}^\ell)^t - (w_{i,j,\alpha}^\ell)^0| = \begin{cases} \mathcal{O}(c^{-1}) & \text{if } \ell = 1 \text{ or } \ell = L \\ \mathcal{O}(c^{-3/2}) & \text{otherwise} \end{cases} \quad (6)$$

where t denotes the gradient descent iteration, such that the overall change of the parameter vector $\|w - w^0\|_2$ is of order $\mathcal{O}(c^{-1/2})$. Hence, the evolution of the network can be well described by a first order expansion around the random initialization, $z(w^t) \approx z(w^0) + \frac{\delta z}{\delta w}(w^t - w^0)$, where $\frac{\delta z}{\delta w}$ is the Jacobian of the network at initialization. In this regime, the training dynamics reduce to

$$z^{t+1} = z^t + \eta \Theta_L^0 (y - z^t) \quad (7)$$

with $z^0 = z(w^0)$ and the NTK Gram matrix (1 training sample and d outputs) given by

$$\Theta_L^0 = \frac{\delta z}{\delta w} \left(\frac{\delta z}{\delta w} \right)^T \Big|_{w=w^0} \in \text{PSD}_d \quad (8)$$

where PSD_d denotes the space of positive semi-definite matrices with $d \times d$ entries. The NTK $\eta\Theta$ stays constant throughout training as $c \rightarrow \infty$, and can be computed in closed form via the following recursion [14]

$$\begin{cases} \Sigma_{a^\ell} = \mathcal{A}(V(\Sigma_{a^{\ell-1}})) \\ \eta\Theta_\ell = \Sigma_{a^\ell} + \mathcal{A}(V'(\Sigma_{a^{\ell-1}}) \circ \eta\Theta_{\ell-1}) \end{cases} \quad (9)$$

with base case

$$\Sigma_{a^1} = \eta\Theta_1 = \mathcal{A}(xx^T) \quad (10)$$

where \circ denotes element-wise matrix multiplication, and Σ_{a^ℓ} denotes the covariance of the preactivations a_i^ℓ for all $i = 1, \dots, c$. The convolution operator $\mathcal{A} : \text{PSD}_d \mapsto \text{PSD}_d$ related to a filter size of $r \times r$ pixels is defined as [22]

$$[\mathcal{A}(\Sigma)]_{i,j} = \sum_{i',j'} [\Sigma]_{i',j'} \quad (11)$$

where i' and j' indicate the pixels within patches of size $r \times r$ centered at pixels i and j respectively. The maps $V : \text{PSD}_d \mapsto \text{PSD}_d$ and $V' : \text{PSD}_d \mapsto \text{PSD}_d$ is defined by the choice of non-linearity and its derivative as

$$V(\Sigma) = \sigma_w^2 \mathbb{E}_{h \sim \mathcal{N}(0, \Sigma)} \{ \phi(h) \phi(h^T) \} \quad (12)$$

$$V'(\Sigma) = \sigma_w^2 \mathbb{E}_{h \sim \mathcal{N}(0, \Sigma)} \{ \phi'(h) \phi'(h^T) \} \quad (13)$$

which are available in closed form for many popular non-linearities such as ReLU (see Appendix B). The denoising process eq. (7) is identical to the twicing procedure in eq. (5), where the non-local filter W is given by $\eta\Theta_L$. In this case, the size of each patch is given by the network's receptive field, as illustrated in Figure 1. The resulting affinity function depends on the architecture, such as depth,

⁴Although this procedure seems to be linear it is in fact nonlinear due to the dependence of W on y

⁵The learning rate cannot be larger than $\mathcal{O}(c^{-1})$ in order to converge to a global minimum [26]. We have also observed in our experiments using the larger learning rates leads to a divergent output.

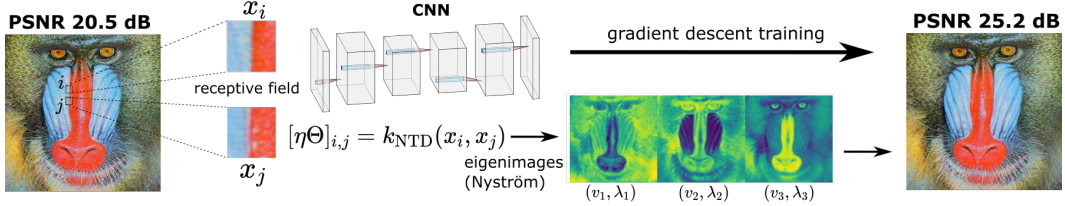


Figure 1: Neural tangent denoising. The denoised baboon is shown for a simple network of a single hidden layer and a kernel of 11×11 pixels. As a comparison, the benchmark denoised CBM3D achieves a PSNR of 25.9 dB for this particular image.

convolution kernel size and choice of non-linearity. For example, a ReLU CNN with a single hidden layer and a convolution kernel size of $r \times r$ pixels has an associated affinity function

$$[\eta\Theta]_{i,j} = k_{\text{NTD}}(x_i, x_j) = \frac{\|x_i\|_2 \|x_j\|_2}{\pi} (\sin(\varphi) + (\pi - \varphi) \cos(\varphi)) \quad (14)$$

with $\varphi = \arccos \frac{x_i^T x_j}{\|x_i\|_2 \|x_j\|_2}$.

4.1 Computing the analytic NTD filter

Instead of training a neural network as in the DIP, we can explicitly compute the filtering matrix $\eta\Theta$, and use eq. (5) to perform the denoising. As the size of the filter matrix ($d \times d$) is prohibitively big to compute and store for large images, we instead only compute a random selection of $m \ll d$ columns of $\eta\Theta$, and approximate the matrix with its leading eigenvalues and eigenimages using the Nyström method [16], as illustrated in Figure 1. The columns are chosen by selecting random pixels uniformly distributed in space, as in the global image denoising algorithm [27]. A detailed description of the algorithm can be found in Appendix G.

5 Adaptive filtering and the deep image prior

5.1 The fixed NTD does not explain the DIP

In the DIP paper, the input is chosen to be random iid noise. In this case, the resulting filter $\eta\Theta$ does not depend in any way on the target image y , where the non-local similarities are computed using the input noise. How bad can this filter be? Applying eq. (9) with noise at the input we get in expectation

$$[\eta\Theta]_{i,j} = \frac{1}{d} \begin{cases} 1 & \text{if } i = j \\ \kappa_L & \text{otherwise} \end{cases} \quad (15)$$

with $\kappa_L \approx 0.25$ for large L , which has a very large first eigenvalue $\lambda_1 = (1 - \kappa_L)/d + \kappa_L \approx 0.25$ associated with a constant image $v_1 = [1, \dots, 1]^T / \sqrt{d}$ and the rest of the eigenvalues of small size $\lambda_i = 0.75/d$ for $i = 2, \dots, d$. Hence, this (linear) filter would just be useful for constant images. In the case of a U-Net with downsampling and upsampling layers, the resulting filter is a crude low-pass filter, but still does not depend on the target image, thus cannot explain the good denoising results obtained by the DIP. However, we believe that this is because the DIP in [6] is not trained with GD but Adam.

5.2 Adaptive filtering with Adam

The Adam optimizer updates the weights according to

$$w^{t+1} = w^t - \eta \frac{\hat{g}_t}{\sqrt{\hat{g}_t^2 + \epsilon}} \quad (16)$$

where \hat{g}_t and \hat{g}_t^2 are running averages of the gradient $\frac{\delta \mathcal{L}}{\delta w}$ and its squared value, computed using hyperparameters β_1 and β_2 , and ϵ is a small scalar to avoid a divergence of the denominator. Removing the adaptation ($\beta_1, \beta_2 \rightarrow 0$) the algorithm reduces to sign gradient descent with learning rate η of

order $\mathcal{O}(c^{-1})$ as in standard gradient descent. Due to this sign property, all weights, including intermediate layers, undergo a larger change than in gradient descent, that is (for t of $\mathcal{O}(1)$)

$$\max_t |(w_{i,j,\alpha}^\ell)^t - (w_{i,j,\alpha}^\ell)^0| = \mathcal{O}(c^{-1}) \quad \forall \ell = 1, \dots, L \quad (17)$$

such that the overall change of the parameter vector $\|w^t - w^0\|_2$ is $\mathcal{O}(1)$, and a Taylor expansion around the initialization does not model accurately the training dynamics⁶. At each iteration, the filter matrix adapts to the target, using non-local information extracted in the backward propagation. The resulting filter is adapted at each iteration, and the process can be written as

$$z^{t+1} = z^t + \eta \Theta_L^t (y - z^t) \quad (18)$$

where the filtering matrix $\eta \Theta_L^t$ adapts according to the residuals $(y - z^t)$, $k = 0, \dots, t$. While a full analysis of the adaptation is out of the scope of this paper, here we provide insight into how the resulting filtering kernel can absorb non-local properties from the target output. Similarly to the output dynamics, the evolution of the preactivations can be well described by its first order expansion:

$$(a_i^\ell)^{t+1} \approx (a_i^\ell)^t - \eta \frac{\delta a_i^\ell}{\delta w} \left(\frac{\delta a_i^\ell}{\delta w} \right)^T \frac{\delta \mathcal{L}}{\delta a_i^\ell} \quad (19)$$

$$\approx (a_i^\ell)^t - \eta \Theta_\ell^t (\delta_i^\ell)^t \quad (20)$$

where the error gradient at layer ℓ and channel i is defined as $\delta_i^\ell \stackrel{\text{def}}{=} \frac{\delta \mathcal{L}}{\delta a_i^\ell} \in \mathbb{R}^d$. As the number of channels goes to infinity, if we treat the δ_i^ℓ as independent of the pre-activations a_i^ℓ computed in the forward pass [22; 19], the gradients of a given layer can still be described by a Gaussian multivariate distribution. This vector carries non-local information (via the operator \mathcal{A}) about the target y , with covariance given by the recursion⁷

$$\Sigma_{\delta^\ell} = \mathcal{A}(\Sigma_{\delta^{\ell+1}}) \circ V'(\Sigma_{a^\ell}) \quad (21)$$

starting with

$$\Sigma_{\delta^{L-1}} = c^{-1} \mathcal{A}((y - z^t)(y - z^t)^T) \circ V'(\Sigma_{a^{L-1}}) \quad (22)$$

which depends on the target image via the residual $(y - z^t)$. In the case of gradient descent training, the change in the preactivations from initialization is negligible as the error terms δ_i^ℓ are of order $\mathcal{O}(c^{-1/2})$ due to the c^{-1} scaling in eq. (22). However, the larger change in intermediate layers when using Adam yields a non-negligible change in the preactivations. While the sign property is responsible for modifying the kernel at initialization, the exact adaptation depends on the choice of hyperparameters β_1 and β_2 .

6 Experiments

We analyze the performance of denoising neural networks both with the corrupted image or iid noise at the input of the network on a standard dataset of 9 color images [9] corrupted with Gaussian noise of $\sigma = 25$. We evaluate 2 different architectures, a simple vanilla CNN with a single hidden layer and a kernel size of 11×11 pixels, and a U-Net with 3 downsampling and upsampling stages (no skip connections) and a kernel size of 3×3 pixels. Both architectures use ReLU non-linearities. A detailed description of the chosen architectures can be found in Appendix H. For each combination of input and architecture, we optimize the network using Adam with standard hyperparameters ($\beta_1 = 0.9$ and $\beta_2 = 0.999$) and vanilla gradient descent (no momentum). We also include results achieved by taking the infinite channel limit of the vanilla CNN, and computing the associated NTD filter. In this case, we use the Nyström approximation to reduce the memory requirements of storing the full matrix $\eta \Theta$. We found that computing only 2% of its columns gives a negligible reduction of performance with respect to computing the full matrix. In the experiments with the image at the input, we remove the random initial output by redefining the network function as $\tilde{z} = z - z^0$ with a fixed translation z^0 , such that $\tilde{z}^0 = 0$ (as with standard twicing). In all experiments, we run the optimization until there is no further improvement of the peak-to-signal-ratio (PSNR)⁸ or a maximum of 10^6 iterations is reached, and keep the best performing output.

⁶Note that a higher order expansion [28] cannot explain the good performance of the DIP, as higher order derivatives are still independent of the target. Moreover, the Hessian would not describe $\mathcal{O}(1)$ perturbations.

⁷A full derivation of eq. (21) is provided in Appendix C.

⁸While we use the oracle image for a fair comparison of all methods, a SURE estimator of the mean squared error [29] could be used in practical applications.

	Vanilla CNN		U-Net	
	Noise	Image	Noise	Image
Adam	19.6	27.4	29.2	29.3
Gradient descent	15.2	27.5	15.0	26.8
Nyström	15.2	28.3	-	-

Table 1: Average peak-signal-to-noise ratio (PSNR) [dB] achieved by different combinations of network architecture, input and optimizer on the dataset of 9 color images [9].

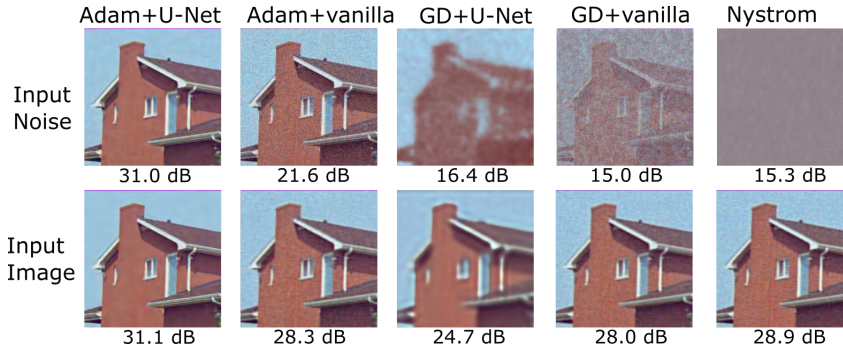


Figure 2: Results for the ‘house’ image. PSNR values are reported below each restored image. The best results are obtained by a U-Net trained with Adam, which is able to provide smoother estimates while preserving sharp edges. However, it provides worse estimates of images with noise-like textures, such as the ‘baboon’ image (see Appendix I).

6.1 Denoising performance

The average PSNR obtained by all possible configurations is shown in Table 1. The results for one of images in the dataset are shown in Figure 2. The best performances are achieved by the U-Net architecture optimized with Adam, followed by the induced filter of the vanilla CNN, computed with Nyström approximation. It is worth noting that while the U-Net in the DIP uses batch normalization, biases, leaky ReLUs instead of ReLUs and a Swish activation function at the output, it does not perform significantly better without them (same average PSNR as the results reported in [6] and 0.1 dB improvement when placing the corrupted image at the input). Furthermore, the best results are obtained when placing the image at the input, without requiring the carefully-designed loss of Noise2Void [4] and Noise2Self [5]. As predicted in Section 5.1, gradient descent provides very poor reconstructions when inputting noise, but improves considerably with the corrupted image as the input. Interestingly, the NTD filter (fixed via gradient descent) induced by the vanilla architecture performs better than its U-Net counterpart. Despite having a larger receptive field (i.e., comparing larger patches), we observed that the U-Net’s eigenimages are more blurry than the vanilla CNN. While the Nyström approximation and a vanilla CNN trained with gradient descent should in theory perform the same, the difference can be attributed to Nyström’s lower rank approximation. Even though Adam plays a big role in adapting the U-Net filter (8 hidden layers), it does not modify significantly the NTD associated with a single hidden layer vanilla CNN. Denoising using the analytic filter takes an average of 52 seconds per image⁹, while training the U-Net with Adam required 806 seconds. Finally, we evaluate the performance of the kernel generated by Adam: denoising with this fixed kernel obtains an average PSNR of 29.3 dB (see Appendix I).

6.2 Change of weights during training

Figure 3 shows the PSNR obtained on the house image, and the change of weights in intermediate layers, $\|w^t - w^0\|_2$ and $\sum_{\ell} \frac{1}{L} \max_{i,j,\alpha} |(w_{i,j,\alpha}^{\ell})^t - (w_{i,j,\alpha}^{\ell})^0|$ as a function of the number of channels when applying gradient descent and Adam with a U-Net architecture. For Adam, the denoising performance only improves as the number of channels increases, suggesting that the adaptive kernel property is not due to a finite network effect. As predicted in Section 5, when using Adam the weights in intermediate layers suffer a change of $\mathcal{O}(1)$ with respect to the ℓ_2 norm, hence adapting

⁹All the experiments were run with a GPU NVIDIA GTX 1080 Ti using the PyTorch library.

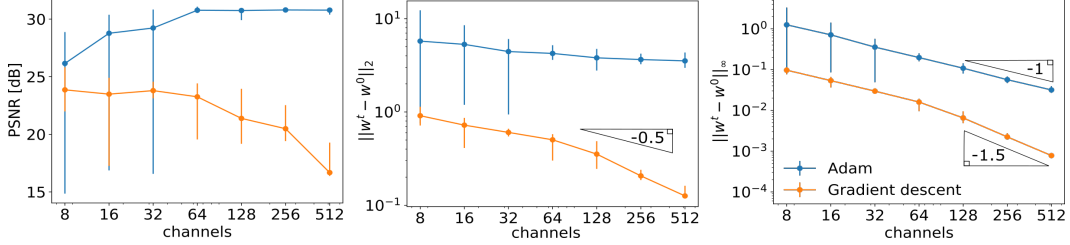


Figure 3: Comparison of Adam and gradient descent training of a U-Net with noise at the input as a function of the number of channels. The PSNR achieved by each method for the ‘house’ image is shown on the left plot, whereas the average ℓ_2 and ℓ_∞ change of weights in hidden layers is shown on the center and right plots respectively. The error bars denote the maximum and minimum values obtained in 10 Monte Carlo repetitions.

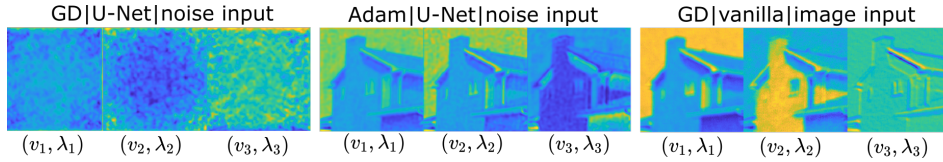


Figure 4: First 3 leading eigenvectors of the covariance of the last preactivations, $\Sigma_{\alpha^{L-1}}$, after 500 iterations of training with Adam or gradient descent with different inputs (noise or image).

the filter at initialization, whereas gradient descent attains a change of the order $\mathcal{O}(c^{-1})$, which corresponds to a fixed filter as $c \rightarrow \infty$. Furthermore, all individual weights incur a similar small change of order $\mathcal{O}(c^{-1/2})$ during training with Adam, suggesting that each weight induces a similar (small) contribution to the network output, in contrast with standard sparsity arguments where only a few weights play a non-negligible (e.g., convolutional sparse coding [30]). Finally, Figure 4 shows the leading eigenvectors of the preactivations of the final hidden layer after 500 iterations of training with gradient descent and Adam. As explained in Section 5, gradient descent does not modify the distribution of the preactivations during training, hence they remain non-informative if noise is placed at the input of the network. However, they carry non-local information when the image is placed at the input. On the other hand, Adam, even with noise at the input, modifies the initial non-informative distribution with non-local features extracted from the target. It is worth noting that traditional patch-based methods also apply adaptive filtering to improve their performance, e.g., BM3D recomputes affinities between patches using a pre-filtered image [9].

7 Conclusions

We introduced a novel analysis of CNN denoisers trained with a single corrupted image, using the recent discovery of the neural tangent kernel to elucidate the strong links with non-local patch-based filtering methods. As the number of channels of the network tends to infinity, the associated pixel affinity function is available in closed form, thus we can study the properties of the induced filter and avoid training a very large network. These results bring insight about the inductive bias of CNNs in image processing problems: The effective degrees of freedom are significantly smaller than the actual number of weights in the network, being fully characterized by the architecture and initialization of the network.

While the NTK theory accurately predicts the behaviour of networks trained with standard gradient descent, we show that it fails to describe the induced filter when training with the popular Adam optimizer. Interestingly, while Adam and other adaptive gradient optimizers are known to provide worse results than stochastic gradient descent in random features models [31], they play a key role here by adapting the filter with non-local information about the target image in the context of the deep image prior. We believe that understanding better the dynamics and hence the inductive bias of this optimizer (and other similar adaptive gradient methods), will be a very important step for improving our understanding of CNN models, both for denoising and more general imaging and image analysis problems.

References

- [1] Morteza Mardani, Qingyun Sun, David Donoho, Vardan Pappyan, Hatf Monajemi, Shreyas Vasanaawala, and John Pauly. Neural proximal gradient descent for compressive imaging. In S. Bengio, H. Wallach, H. Larochelle, K. Grauman, N. Cesa-Bianchi, and R. Garnett, editors, *Advances in Neural Information Processing Systems 31*, pages 9573–9583. Curran Associates, Inc., 2018. URL <http://papers.nips.cc/paper/8166-neural-proximal-gradient-descent-for-compressive-imaging.pdf>.
- [2] J. Liu, Y. Sun, C. Eldeniz, W. Gan, H. An, and U. S. Kamilov. Rare: Image reconstruction using deep priors learned without ground truth. *IEEE Journal of Selected Topics in Signal Processing*, pages 1–1, 2020.
- [3] Jaakko Lehtinen, Jacob Munkberg, Jon Hasselgren, Samuli Laine, Tero Karras, Miika Aittala, and Timo Aila. Noise2Noise: Learning image restoration without clean data. In Jennifer Dy and Andreas Krause, editors, *Proceedings of the 35th International Conference on Machine Learning*, volume 80 of *Proceedings of Machine Learning Research*, pages 2965–2974, Stockholm, Sweden, 10–15 Jul 2018. PMLR. URL <http://proceedings.mlr.press/v80/lehtinen18a.html>.
- [4] A. Krull, T. Buchholz, and F. Jug. Noise2void - learning denoising from single noisy images. In *2019 IEEE/CVF Conference on Computer Vision and Pattern Recognition (CVPR)*, pages 2124–2132, 2019.
- [5] Joshua Batson and Loic Royer. Noise2Self: Blind denoising by self-supervision. In Kamalika Chaudhuri and Ruslan Salakhutdinov, editors, *Proceedings of the 36th International Conference on Machine Learning*, volume 97 of *Proceedings of Machine Learning Research*, pages 524–533, Long Beach, California, USA, 09–15 Jun 2019. PMLR. URL <http://proceedings.mlr.press/v97/batson19a.html>.
- [6] Dmitry Ulyanov, Andrea Vedaldi, and Victor Lempitsky. Deep image prior. In *Proceedings of the IEEE Conference on Computer Vision and Pattern Recognition*, pages 9446–9454, 2018.
- [7] Olaf Ronneberger, Philipp Fischer, and Thomas Brox. U-net: Convolutional networks for biomedical image segmentation. In Nassir Navab, Joachim Hornegger, William M. Wells, and Alejandro F. Frangi, editors, *Medical Image Computing and Computer-Assisted Intervention – MICCAI 2015*, pages 234–241, Cham, 2015. Springer International Publishing. ISBN 978-3-319-24574-4.
- [8] Antoni Buades, Bartomeu Coll, and J-M Morel. A non-local algorithm for image denoising. In *2005 IEEE Computer Society Conference on Computer Vision and Pattern Recognition (CVPR'05)*, volume 2, pages 60–65. IEEE, 2005.
- [9] Kostadin Dabov, Alessandro Foi, Vladimir Katkovnik, and Karen Egiazarian. Image denoising by sparse 3-d transform-domain collaborative filtering. *IEEE Transactions on image processing*, 16(8):2080–2095, 2007.
- [10] Yaniv Romano, Michael Elad, and Peyman Milanfar. The little engine that could: Regularization by denoising (RED). *SIAM Journal on Imaging Sciences*, 10(4):1804–1844, 2017. doi: 10.1137/16M1102884. URL <https://doi.org/10.1137/16M1102884>.
- [11] Singanallur V Venkatakrishnan, Charles A Bouman, and Brendt Wohlberg. Plug-and-play priors for model based reconstruction. In *2013 IEEE Global Conference on Signal and Information Processing*, pages 945–948. IEEE, 2013.
- [12] Chiyuan Zhang, Samy Bengio, Moritz Hardt, Benjamin Recht, and Oriol Vinyals. Understanding deep learning requires rethinking generalization. *arXiv preprint arXiv:1611.03530*, 2016.
- [13] Arthur Jacot, Franck Gabriel, and Clement Hongler. Neural tangent kernel: Convergence and generalization in neural networks. In S. Bengio, H. Wallach, H. Larochelle, K. Grauman, N. Cesa-Bianchi, and R. Garnett, editors, *Advances in Neural Information Processing Systems 31*, pages 8571–8580. Curran Associates, Inc., 2018. URL <http://papers.nips.cc/paper/8076-neural-tangent-kernel-convergence-and-generalization-in-neural-networks.pdf>.

- [14] Sanjeev Arora, Simon S Du, Wei Hu, Zhiyuan Li, Russ R Salakhutdinov, and Ruosong Wang. On exact computation with an infinitely wide neural net. In H. Wallach, H. Larochelle, A. Beygelzimer, F. d’Alche Buc, E. Fox, and R. Garnett, editors, *Advances in Neural Information Processing Systems 32*, pages 8141–8150. Curran Associates, Inc., 2019. URL <http://papers.nips.cc/paper/9025-on-exact-computation-with-an-infinitely-wide-neural-net.pdf>.
- [15] Peyman Milanfar. A tour of modern image filtering: New insights and methods, both practical and theoretical. *IEEE Signal Processing Magazine*, 30(1):106–128, 2012.
- [16] Christopher K. I. Williams and Matthias Seeger. Using the nystrom method to speed up kernel machines. In T. K. Leen, T. G. Dietterich, and V. Tresp, editors, *Advances in Neural Information Processing Systems 13*, pages 682–688. MIT Press, 2001. URL <http://papers.nips.cc/paper/1866-using-the-nystrom-method-to-speed-up-kernel-machines.pdf>.
- [17] Radford M Neal. *Bayesian learning for neural networks*. PhD thesis, University of Toronto, 1995.
- [18] Roman Novak, Lechao Xiao, Yasaman Bahri, Jaehoon Lee, Greg Yang, Daniel A. Abolafia, Jeffrey Pennington, and Jascha Sohl-dickstein. Bayesian deep convolutional networks with many channels are gaussian processes. In *International Conference on Learning Representations*, 2019. URL <https://openreview.net/forum?id=B1g30j0qF7>.
- [19] Greg Yang. Scaling Limits of Wide Neural Networks with Weight Sharing: Gaussian Process Behavior, Gradient Independence, and Neural Tangent Kernel Derivation. *arXiv e-prints*, art. arXiv:1902.04760, February 2019.
- [20] Z. Cheng, M. Gadelha, S. Maji, and D. Sheldon. A bayesian perspective on the deep image prior. In *2019 IEEE/CVF Conference on Computer Vision and Pattern Recognition (CVPR)*, pages 5438–5446, 2019.
- [21] Kaiming He, Xiangyu Zhang, Shaoqing Ren, and Jian Sun. Delving deep into rectifiers: Surpassing human-level performance on ImageNet classification. In *The IEEE International Conference on Computer Vision (ICCV)*, December 2015.
- [22] Lechao Xiao, Yasaman Bahri, Jascha Sohl-Dickstein, Samuel S Schoenholz, and Jeffrey Pennington. Dynamical isometry and a mean field theory of CNNs: How to train 10,000-layer vanilla convolutional neural networks. *arXiv preprint arXiv:1806.05393*, 2018.
- [23] Diederik P. Kingma and Jimmy Ba. Adam: A method for stochastic optimization. In Yoshua Bengio and Yann LeCun, editors, *3rd International Conference on Learning Representations, ICLR 2015, San Diego, CA, USA, May 7-9, 2015, Conference Track Proceedings*, 2015. URL <http://arxiv.org/abs/1412.6980>.
- [24] H. Takeda, S. Farsiu, and P. Milanfar. Kernel regression for image processing and reconstruction. *IEEE Transactions on Image Processing*, 16(2):349–366, 2007.
- [25] Jaehoon Lee, Lechao Xiao, Samuel Schoenholz, Yasaman Bahri, Roman Novak, Jascha Sohl-Dickstein, and Jeffrey Pennington. Wide neural networks of any depth evolve as linear models under gradient descent. In H. Wallach, H. Larochelle, A. Beygelzimer, F. d’Alche Buc, E. Fox, and R. Garnett, editors, *Advances in Neural Information Processing Systems 32*, pages 8572–8583. Curran Associates, Inc., 2019.
- [26] Ryo Karakida, Shotaro Akaho, and Shun-ichi Amari. Universal statistics of fisher information in deep neural networks: Mean field approach. In Kamalika Chaudhuri and Masashi Sugiyama, editors, *Proceedings of Machine Learning Research*, volume 89 of *Proceedings of Machine Learning Research*, pages 1032–1041. PMLR, 16–18 Apr 2019. URL <http://proceedings.mlr.press/v89/karakida19a.html>.
- [27] H. Talebi and P. Milanfar. Global image denoising. *IEEE Transactions on Image Processing*, 23(2):755–768, 2014.

- [28] Yu Bai, Ben Krause, Huan Wang, Caiming Xiong, and Richard Socher. Taylorized Training: Towards Better Approximation of Neural Network Training at Finite Width. *arXiv e-prints*, art. arXiv:2002.04010, February 2020.
- [29] S. Ramani, T. Blu, and M. Unser. Monte-Carlo SURE: A black-box optimization of regularization parameters for general denoising algorithms. *IEEE Transactions on Image Processing*, 17(9):1540–1554, 2008.
- [30] B. Wohlberg. Efficient algorithms for convolutional sparse representations. *IEEE Transactions on Image Processing*, 25(1):301–315, 2016.
- [31] Ashia C Wilson, Rebecca Roelofs, Mitchell Stern, Nati Srebro, and Benjamin Recht. The marginal value of adaptive gradient methods in machine learning. In I. Guyon, U. V. Luxburg, S. Bengio, H. Wallach, R. Fergus, S. Vishwanathan, and R. Garnett, editors, *Advances in Neural Information Processing Systems 30*, pages 4148–4158. Curran Associates, Inc., 2017.
- [32] Youngmin Cho and Lawrence K Saul. Kernel methods for deep learning. In *Advances in neural information processing systems*, pages 342–350, 2009.

A Assumptions and other observations

1. We have omitted the use of biases to simplify the presentation. In the case of ReLU non-linearities, the presence of biases would add an additional constant term to the V and V' maps in eqs. (35) and (46) [14]. We also found that the denoising performance did not vary significantly with or without them in the case of ReLU non-linearities.
2. We focus on the case where all hidden layers have the same number of channels c . Our analysis can be easily extended for different number of channels per layer, as long as they all grow at the same rate when taking $c \rightarrow \infty$ [26].
3. Despite we assume that the output z has a single channel for the main derivations, the theory applies to a variable number of channels c_L , as long as they are significantly smaller than the ones of the hidden layers c . The extension to multiple channels is provided in appendix E.
4. We drop the dependence of the pre-activations a^ℓ of the input x to lighten notations.
5. For ease of presentation, we focus on the case where all layers have the same image size $d_\ell = d$. Appendix F extends the results for downsampling and upsampling layers of a U-Net architecture.
6. It is worth noting that some architectures proposed in the deep image prior paper [6] have c_0 of order c . However, we noticed that reducing the number of channels does not impact significantly the performance.
7. The theory presented here cannot not be straightforwardly applied to networks with batch normalization and max pooling. However, we noted that they do not affect significantly the denoising performance of the networks.

B Forward signal propagation

In this section we study the statistics of the signal as it propagates through the neural network. As $c \rightarrow \infty$, the preactivations at each layer a_i^ℓ can be well described by a multivariate distribution due to the central limit theorem [17]. Hence, computing the mean and covariance is enough to fully characterize their distribution.

For the first hidden layer we have for each channel $i = 1, \dots, c$

$$\mu_{a^1} = \mathbb{E}\{W_{i,1}^1\} \mathbb{E}\{x\} \tag{23}$$

$$= 0 \tag{24}$$

and covariance

$$\Sigma_{a^1} = \mathbb{E}\{W_{i,1}^1 x x^T (W_{i,1}^1)^T\} \tag{25}$$

where the independence of weights across different filters was used to simplify the sum. Note that we have dropped the dependence of the mean and covariance on the specific channel i , as all channels share the same mean and covariance. The expression in eq. (25) consists of pairwise expectations

$$\mathbb{E}\{[W_{i,j}^\ell x]_\mu [W_{i,j}^\ell x]_v\} = \sum_{\mu', v'} \mathbb{E}\{x_{\mu'} x_{v'}\} \quad (26)$$

where μ' and v' are the indices of pixels within patches centered at μ and v respectively. It can be written in a more compact form as

$$\Sigma_{a^\ell} = \mathcal{A}(xx^T) \quad (27)$$

where the convolution map $\mathcal{A} : \text{PSD}_n \mapsto \text{PSD}_n$ is defined as [22]

$$[\mathcal{A}(\Sigma)]_{\mu, v} = \sum_{\mu', v'} [\Sigma]_{\mu', v'} \quad (28)$$

For the following layers we also have zero mean, i.e.,

$$\mu_{a^\ell} = \sum_{j=1}^c \mathbb{E}\{W_{i,j}^\ell\} \mathbb{E}\{\phi(a_j^{\ell-1})\} \quad (29)$$

$$= 0 \quad (30)$$

and a covariance is given by

$$\Sigma_{a^\ell} = \sum_{j=1}^c \mathbb{E}\{W_{i,j}^{\ell-1} \phi(a_j^{\ell-1}) \phi(a_j^{\ell-1})^T (W_{i,j}^{\ell-1})^T\} \quad (31)$$

where the first term of the right hand side is given by

$$\mathbb{E}\{[W_{i,j}^\ell \phi(a_j^{\ell-1})]_\mu [W_{i,j}^\ell \phi(a_j^{\ell-1})]_v\} = \sum_{\mu', v'} \mathbb{E}\{\phi(a_{j,\mu'}^{\ell-1}) \phi(a_{j,v'}^{\ell-1})\} \quad (32)$$

The expression can be written in compact form as

$$\Sigma_{a^\ell} = \mathcal{A}(V(\Sigma_{a^{\ell-1}})) \quad (33)$$

where the map $V : \text{PSD}_n \mapsto \text{PSD}_n$ linked to a non-linearity $\phi(x)$ is defined as

$$V(\Sigma) = \mathbb{E}_{h \sim \mathcal{N}(0, \Sigma)} \{\phi(h) \phi(h^T)\} \quad (34)$$

The V -map consists of two-dimensional integrals that are available in closed-form for many activation functions. In the case of ReLU non-linearities, we have [32]

$$[V(\Sigma)]_{\mu, v} = \frac{\sqrt{\Sigma_{\mu, \mu} \Sigma_{v, v}}}{\pi} (\sin(\varphi) + (\pi - \varphi) \cos(\varphi)) \quad (35)$$

where $\varphi = \arccos(\Sigma_{\mu, v} / \sqrt{\Sigma_{\mu, \mu} \Sigma_{v, v}})$. As discussed in [22], ℓ repeated applications of the operator given by eq. (35) quickly converge to a matrix of the form

$$[\Sigma]_{\mu, v} = \begin{cases} 1 & \text{if } \mu = v \\ \kappa_\ell & \text{otherwise} \end{cases} \quad (36)$$

where κ_ℓ decreases to zero exponentially fast with depth. Note that the matrix in eq. (36) is invariant to the \mathcal{A} map, as the diagonal elements are averaged with other diagonal elements, whereas the off-diagonal entries are averaged with other off-diagonal ones.

The output z is also characterized by a multivariate Gaussian distribution with

$$\Sigma_z = \mathcal{A}(V(\Sigma_{a^{L-1}})). \quad (37)$$

The main difference between the fully connected and convolutional architectures lies in the covariance Σ_{a^ℓ} . In the fully connected case, \mathcal{A} boils down to the identity operator, and Σ_{a^ℓ} has an isotropic structure for all layers, whereas the convolutional network presents rich covariances within the pixels of each channel in eq. (31), as \mathcal{A} cross-correlates different patches of the image.

B.1 Gaussian Process interpretation

We can use the distribution of a infinite neural network at initialization to define a prior $p(z) = \mathcal{N}(0, \Sigma_z)$ from a Bayesian inference viewpoint [17], a strategy named the Bayesian deep image prior in [20]. In the case of standard Gaussian noise $z = y + n$ we have

$$y|z \sim \mathcal{N}(z, \sigma_n^2 I) \quad (38)$$

$$z \sim \mathcal{N}(0, \Sigma_z) \quad (39)$$

where the posterior distribution is available in closed form

$$z|y \sim \mathcal{N}((I + \sigma_n^2 \Sigma_z^{-1})^{-1} z, (I \sigma_n^{-2} + \Sigma_z^{-1})^{-1}) \quad (40)$$

Note that, if iid noise is placed at the input of the network, Σ_z does not depend on the noise image z in any way. Moreover, for a ReLU network, this covariance is given by eq. (36). Figure 5 shows that the off-diagonal elements κ_L tend to 1 as the network becomes larger. This prior just promotes constant images.

C Backward signal propagation

A similar analysis can be made for the propagation of gradients through the network in backwards direction. This is especially useful to study the behaviour of backpropagation training and avoid vanishing or exploding gradients in deep networks. Computing gradients with respect to the weights of the ℓ th layer can be done using the chain rule:

$$\frac{\delta \mathcal{L}}{\delta w^\ell} = \frac{\delta \mathcal{L}}{\delta z} \frac{\delta z}{\delta a^{L-1}} \cdots \frac{\delta a^{\ell+1}}{\delta a^\ell} \frac{\delta a^\ell}{\delta w^\ell} \quad (41)$$

We define the gradient as:

$$\delta_i^\ell \stackrel{\text{def}}{=} \frac{\delta \mathcal{L}}{\delta z} \frac{\delta z}{\delta a^{L-1}} \cdots \frac{\delta a^\ell}{\delta a_i^{\ell-1}} \in \mathbb{R}^d \quad (42)$$

with $\delta^L \stackrel{\text{def}}{=} \frac{\delta \mathcal{L}}{\delta z}$. For a squared loss, the gradient at the last layer is

$$\delta^L = z - y. \quad (43)$$

Assuming that independence between gradients and preactivations [22]¹⁰, we have for each channel $i = 1, \dots, c$ of layer $L - 1$

$$\delta_i^{L-1} = \text{diag}(\phi'(a_i^{L-1})) (W_{1,i}^L)^T \delta^L \quad (44)$$

which has zero mean and covariance given by

$$\Sigma_{\delta^{L-1}} = \frac{1}{c} V'(\Sigma_{a^{L-1}}) \circ \mathcal{A}(\Sigma_{\delta^L}) \quad (45)$$

where the map $V' : \text{PSD}_n \mapsto \text{PSD}_n$ is defined as

$$V'(\Sigma) = 2\mathbb{E}_{h \sim \mathcal{N}(0, \Sigma)} \{\phi'(h) \phi'(h^T)\} \quad (46)$$

The expected values are available in closed form for many non-linearities. We can use the following recursive formula to compute the rest of the layers $\ell = L - 2, \dots, 1$

$$\delta_i^\ell = \sum_{j=1}^{C^\ell} \text{diag}(\phi'(a_i^{\ell-1})) (W_{j,i}^\ell)^T \delta_j^{\ell+1} \quad (47)$$

Computing the propagation recursively in backwards direction, we have $\mu_{\delta^\ell} = 0$ and covariance

$$\Sigma_{\delta_i^\ell} = \mathcal{A}(\Sigma_{\delta^{\ell+1}}) \circ V'(\Sigma_{a^\ell}) \quad (48)$$

For ReLU non-linearities the V' map is computed as

$$[V'(\Sigma)]_{\mu,v} = 1 - \frac{1}{\pi} \arccos \frac{\Sigma_{\mu,v}}{\sqrt{\Sigma_{\mu,\mu} \Sigma_{v,v}}} \quad (49)$$

which as with the V counterpart¹¹, repeated applications of this map converge exponentially fast to the simple matrix structure in eq. (36).

¹⁰This assumption is formally justified a recent work [19].

¹¹Note that the discontinuity of the ReLU function at 0 is unimportant here due to the expectation operator.

D Neural Tangent Kernel

In this section, we will denote all the trainable network parameters at iteration t as w^t . Consider training a network via gradient descent¹², that is

$$w^{t+1} = w^t - \eta \frac{\delta \mathcal{L}}{\delta w}(w^t) \quad (50)$$

We can study the evolution of the function defined by the weights $z^t \stackrel{\text{def}}{=} z(w^t)$, using a first order Taylor expansion, i.e.,

$$z^{t+1} \approx z(w^t) + \frac{\delta z}{\delta w}(w^{t+1} - w^t) \quad (51)$$

$$\approx z^t - \eta \frac{\delta z}{\delta w} \frac{\delta \mathcal{L}}{\delta w} \quad (52)$$

$$\approx z^t - \eta \frac{\delta z}{\delta w} \left(\frac{\delta z}{\delta w} \right)^T \frac{\delta \mathcal{L}}{\delta z} \quad (53)$$

where we have used eq. (50) in the second line and the chain rule in the third line. The neural tangent kernel (NTK) is given by

$$\Theta_L = \frac{\delta z}{\delta w} \left(\frac{\delta z}{\delta w} \right)^T \quad (54)$$

$$= \sum_{\ell, i, j, \alpha} \frac{\delta z}{\delta w_{i, j, \alpha}^\ell} \left(\frac{\delta z}{\delta w_{i, j, \alpha}^\ell} \right)^T \quad (55)$$

We can start with the base case,

$$\Theta_1 = c \mathcal{A}(xx^T) \quad (56)$$

and notice the following recursive formulation

$$\Theta_\ell = \frac{\delta a_i^\ell}{\delta w^\ell} \left(\frac{\delta a_i^\ell}{\delta w^\ell} \right)^T + \frac{\delta a_i^\ell}{\delta a^{\ell-1}} \Theta_{\ell-1} \left(\frac{\delta a_i^\ell}{\delta a^{\ell-1}} \right)^T \quad (57)$$

$$= \sum_{j=1}^c \mathcal{A} \left(\phi(a_j^{\ell-1}) \phi(a_j^{\ell-1})^T \right) + W_{i, j}^\ell \text{diag}(\phi'(a_j^{\ell-1})) \Theta_{\ell-1} \text{diag}(\phi'(a_j^{\ell-1})) (W_{i, j}^\ell)^T \quad (58)$$

where w^ℓ denotes the weights corresponding to layer ℓ . The learning rate η is chosen of order $\mathcal{O}(c^{-1})$, in order to converge to global minimum [26]. Without loss of generality, we use $\eta = \gamma c^{-1}$ for the following derivations, where γ is $\mathcal{O}(1)$ and chosen such that the neural tangent kernel has its eigenvalues bounded by 1. As shown in [19], for an infinite number of channels $c \rightarrow \infty$, due to the law of large numbers we have

$$\eta \Theta_\ell = \Sigma_{a^\ell} + \mathcal{A}(V'(\Sigma_{a^\ell}) \circ \eta \Theta_{\ell-1}) \quad (59)$$

which is a fixed (deterministic) matrix. As a function of the input image (or noise) patches, the NTK defines a kernel acting on pairs of input patches x_1 and x_2 , i.e., $k(x_1, x_2) : \mathbb{R}^{d_0} \times \mathbb{R}^{d_0} \mapsto \mathbb{R}_+$. As discussed in the main paper, if iid noise is placed at the input, the resulting Gram matrix is given by eq. (36) with κ_L as shown in Figure 5.

For a squared loss $\mathcal{L} = \frac{1}{2} \|z - y\|_2^2$, the dynamics of eq. (51) can be written as

$$z^{t+1} = z^t + \eta \Theta_L (y - z^t) \quad (60)$$

$$= (I - \eta \Theta)^{t+1} z^0 + \sum_{k=1}^t (\eta \Theta_L)^k y \quad (61)$$

with initial condition z^0 given by the Gaussian Process initialization described in Appendix B. The expression for z^t can be simplified further by noting that the learning rate has to be chosen such that

¹²A very similar analysis can be done for gradient flow and stochastic gradient descent [25]

$\eta\Theta$ has its eigenvalues bounded from above by 1 (to avoid a diverging gradient descent). Hence, as $I - \eta\Theta$ is invertible, we can apply the geometric series formula

$$z^t = (I - \eta\Theta_L)^t z^0 + (I - \eta\Theta_L)^{-1} (I - (\eta\Theta_L)^t) y \quad (62)$$

Note that the only random component of this equation is the GP initialization z^0 . As z^t is an affine transformation of a Gaussian process, it is also itself a Gaussian process for every iteration t . Hence, we have

$$z^t \sim \mathcal{N}((I - \eta\Theta)^{-1} (I - (\eta\Theta)^t) y, (I - \eta\Theta_L)^t \Sigma_z (I - \eta\Theta)^t) \quad (63)$$

It is easy to see that z^t converges at an exponential rate towards a singular distribution centered at y as $t \rightarrow \infty$.

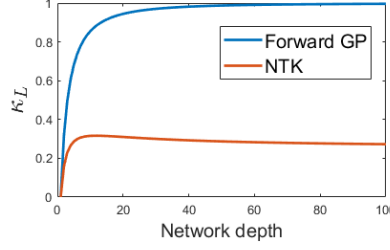


Figure 5: Off-diagonal elements of the filtering matrix associated with the Gaussian Process at initialization and the neural tangent kernel.

E Multiple input and output channels

The theory applies for any number of input and output channels, as long as they are much smaller than the number of hidden channels c . A multi-channel input modifies the computation in the first layer eq. (25). In this case, first multiplying the patches channel-wise and then summing the result, that is

$$\Sigma_{a^1} = \sum_{j=0}^{c_0} \mathbb{E}\{W_{i,j}^1 x_j x_j^T (W_{i,j}^1)^T\} \quad (64)$$

where x_j denotes the j th channel of the input, and the corresponding infinite-width operator is computed as

$$\Sigma_{a^1} = \sum_{j=0}^{c_0} \mathcal{A}(x_j x_j^T) \quad (65)$$

Hence, the pixel affinity function is now defined for a receptive field d_0 , and patches x_1 and x_2 of c_0 channels as

$$k(x_1, x_2) : \mathbb{R}^{c_0 d_0} \times \mathbb{R}^{c_0 d_0} \mapsto \mathbb{R}_+. \quad (66)$$

Multiple output channels are computed separately using the same filtering matrix, i.e.,

$$z_i^{t+1} = z_i^t + \eta\Theta_L(y - z_i^t) \quad (67)$$

for $i = 1, \dots, c_L$. Note that both the color versions of NLM and BM3D do a similar procedure, computing the filtering matrix with luminance (i.e., a linear combination of the RGB channels), and apply the filtering process to each channel separately.

F Downsampling and upsampling layers

Downsampling can be achieved either via 2-strided convolutional layers or directly with linear downsampling operations, such as bilinear or nearest neighbor downsampling. Strided convolutions are a straightforward extension of the \mathcal{A} operator defined in eq. (28), summing over strided patches instead of contiguous ones. Linear downsampling operations can be expressed as a matrix vector

product applied channel-wise, i.e., $a_i^{\ell+1} = Da_i^\ell$ where $D \in \mathbb{R}^{d \times d/2}$ is a fixed matrix given by downsampler (bilinear, nearest neighbor, etc.). The covariance of $a_i^{\ell+1}$ is then

$$\Sigma_{a^{\ell+1}} = D\Sigma_{a^\ell}D^T. \quad (68)$$

Upsampling is generally performed with bilinear or nearest neighbor layers, as transposed convolutions provide worse results [6]. These are analogous to the downsampling case, but with an upsampling matrix $U \in \mathbb{R}^{d/2 \times d}$, that is

$$\Sigma_{a^{\ell+1}} = U\Sigma_{a^\ell}U^T. \quad (69)$$

G Nyström denoising

The Nystrom method approximates the first m eigenvectors of the NTD matrix by computing only a subset of $m \ll d$ columns [16], i.e., the sub-matrix

$$\Theta_{d,m} = \begin{bmatrix} \Theta_{m,m} \\ \Theta_{d-m,m} \end{bmatrix} \quad (70)$$

We first perform a singular value decomposition of the small sub-matrix $\Theta_{m,m} = \sum_{i=1}^m \tilde{\lambda}_i \tilde{v}_i \tilde{v}_i^T$, and then approximate the eigenvectors and eigenvalues of the full matrix as

$$v_i = \sqrt{\frac{m}{d}} \frac{1}{\tilde{\lambda}_i} \Theta_{d,m} \tilde{v}_i \quad (71)$$

$$\lambda_i = \frac{d}{m} \tilde{\lambda}_i \quad (72)$$

We fix $m = 0.02d$, which allows us to compute most of the md pixel affinities in parallel on the GPU. The selection of columns is done similarly to global image denoising [27], choosing a random selection of pixels uniformly distributed in space. Before applying the denoising procedure, we scale the eigenvalues, such that the maximum eigenvalue is 1.

H Architectures

H.1 Vanilla CNN

Table 2 shows the configuration used for the vanilla CNN results with $c = 512$ channels per hidden layer. The network has a total of 187,392 trainable weights.

Module	Function	Infinite-channel forward operator
input	3 channel RGB image	
conv1	11×11 pixel convolution	\mathcal{A} with $r = 11$
relu1	ReLU activation $\max(x, 0)$	V
conv2	1×1 pixel convolution	\mathcal{A} with $r = 1$
output	3 channel RGB image	

Table 2: Vanilla CNN configuration with a single-hidden layer.

H.2 U-Net

Table 3 shows the configuration used for the U-Net results with $c = 128$ channels per hidden layer. The network has a total of 1,036,032 trainable weights.

I Additional results

In all the denoising experiments, we normalize the corrupted images by subtracting 0.5 from all pixels, such that they defined in the centered interval $[-0.5, 5]$. Before computing the PSNR, we denormalize the images by summing 0.5 to all pixels and clipping, such that all pixels are in the interval $[0, 1]$.

Module	Function	Infinite-channel forward operator
input	3 channel RGB image	
convd1	3×3 convolution	\mathcal{A} with $r = 3$
relu1	ReLU activation $\max(x, 0)$	V
down1	Bilinear downsampling	D
convd2	3×3 convolution	\mathcal{A} with $r = 3$
relu2	ReLU activation $\max(x, 0)$	V
down2	Bilinear downsampling	D
convd3	3×3 convolution	\mathcal{A} with $r = 3$
relu3	ReLU activation $\max(x, 0)$	V
down3	Bilinear downsampling	D
convd4	3×3 convolution	\mathcal{A} with $r = 3$
relu4	ReLU activation $\max(x, 0)$	V
conv4	3×3 convolution	\mathcal{A} with $r = 3$
up1	Bilinear upsampling	U
convu1	3×3 convolution	\mathcal{A} with $r = 3$
relu5	ReLU activation $\max(x, 0)$	V
up2	Bilinear upsampling	U
convu2	3×3 convolution	\mathcal{A} with $r = 3$
relu6	ReLU activation $\max(x, 0)$	V
up3	Bilinear upsampling	U
convu3	3×3 convolution	\mathcal{A} with $r = 3$
relu7	ReLU activation $\max(x, 0)$	V
convu4	1×1 convolution	\mathcal{A} with $r = 1$
output	3 channel RGB image	

Table 3: U-Net configuration with bilinear downsampling and upsampling layers.

I.1 Denoising examples

The deep image prior setting (U-Net, noise input and Adam optimizer), performs very well in images with large piece-wise smooth patches, such as the ‘house’ image shown in the main paper or the ‘F16’ image in Figure 7, but does not provide good reconstructions in images with noise-like textures, as the ‘baboon’ shown in Figure 6. The best performing denoiser for this image is the closed form filter associated with a vanilla CNN, approximated with Nyström.

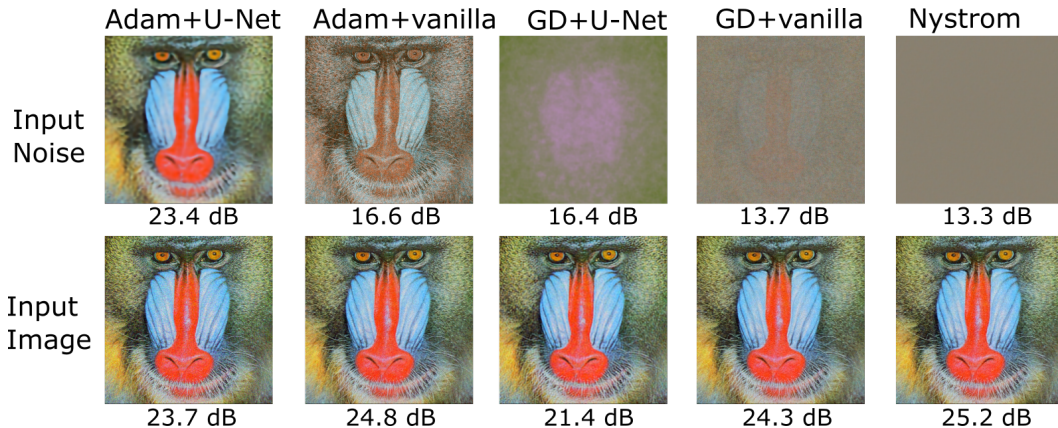


Figure 6: Results for the ‘baboon’ image. PSNR values are reported below each restored image. The best results are obtained by the Nyström approximation of a vanilla CNN filter.

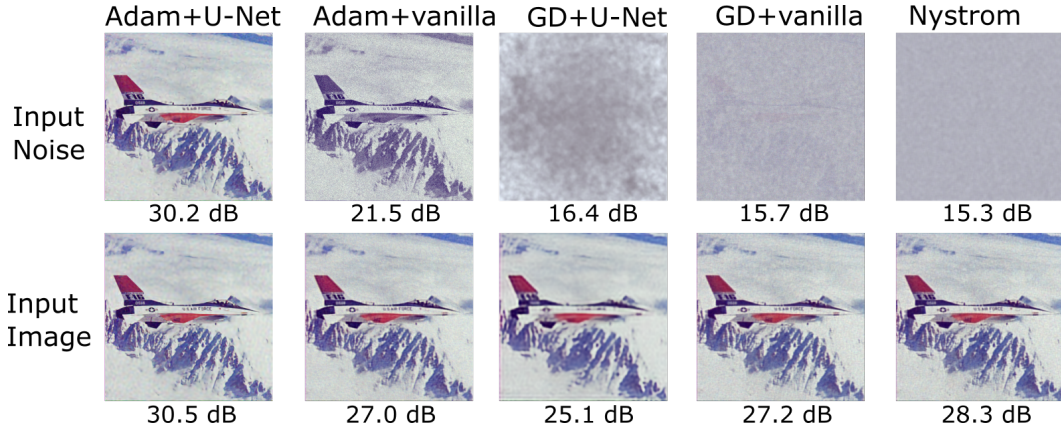


Figure 7: Results for the ‘F16’ image. PSNR values are reported below each restored image. The best results are obtained by a U-Net trained with Adam, which is able to provide smoother estimates while preserving sharp edges.

	U-Net/Adam/noise	U-Net/Adam/image	Vanilla/Nyström/image
$\sigma = 5$	24.4	24.1	22.3
$\sigma = 100$	33.5	35.3	34.5

Table 4: Average PSNR [dB] obtained by the best-performing algorithms for different noise levels.

I.2 Additional noise levels

We evaluate the best-performing denoisers (U-Net with noise or image input trained using Adam and Nyström approximation of a vanilla CNN) for iid Gaussian noise with standard deviations of $\sigma = 5$ (low noise) and $\sigma = 100$ (high noise). Table 4 shows the results for the dataset of 9 color images [9]. Inputting the image when using Adam achieves an improvement of 1.8 dB in the low-noise case, whereas it provides slightly worse (0.3 dB) results in the high noise case.

I.3 Epoch count

Table 5 shows the average epoch-count of all methods for the 9 color image dataset. Inputting the image instead of noise reduces the number of iterations when optimizing with Adam, as the induced filtering matrix is better conditioned. Gradient descent requires much more iterations than Adam as it does not use any momentum. As discussed in the main paper, the filtering matrix associated with a vanilla CNN and noise input is so ill-conditioned that gradient descent does not converge even after 10^6 iterations.

	Vanilla CNN		U-Net	
	Noise	Image	Noise	Image
Adam	145340	64	10248	5088
Gradient descent	$> 10^6$	69526	50355	286042
Nyström	368	504	-	-

Table 5: Average epoch-count by different combinations of network architecture, input and optimizer on the dataset of 9 color images [9].

I.4 Applying the adapted filter

We analyze the performance of the filter obtained by Adam with the corrupted image at the input and U-Net architecture, by rerunning the twicing process with a fixed the kernel. A straightforward way to do this is to compute the NTK obtained by Adam using eq. (54). However, eq. (54) is too computationally intensive to perform in practice. A more plausible option is to use gradient descent, that fixes the kernel throughout training. The procedure can be summarized as follows:

First, the kernel is adapted by applying 5000 iterations of Adam. Then, we remove the output, i.e., $\tilde{z} = z - z^{5000}$, and retrain with gradient descent, which equates to applying a fixed filter but with an adapted kernel, different from the random initialization one. This strategy obtains an average PSNR of 29.3 dB.